

Antiferromagnetism in α - $\text{Li}_3\text{Fe}_2(\text{PO}_4)_3$

J.L. Zarestky^a, D. Vaknin^{a,*}, B.C. Chakoumakos^b, T. Rojo^c, A. Goñi^c,
G.E. Barberis^d

^a Ames Laboratory and Department of Physics and Astronomy, A500, Iowa State University, Ames, IA 50011, USA

^b Oak Ridge National Laboratory, Oak Ridge, TN 37831, USA

^c Departamento Química Inorgánica, Facultad de Ciencias, Universidad del País Vasco/Euskal Herriko, Unibertsitatea, A.P. 644,
48080 Bilbao, Spain

^d Departamento de Eletrônica Quântica, Instituto de Física Gleb Wataghin, Universidade Estadual de Campinas (UNICAMP),
13083-970 Campinas (SP) Brazil

Received 5 March 2001; received in revised form 30 May 2001

Abstract

Neutron diffraction techniques have been used to determine the magnetic structure of Fe in monoclinic α - $\text{Li}_3\text{Fe}_2(\text{PO}_4)_3$. Rietveld analysis of the room temperature powder diffraction pattern confirms the monoclinic structure of the sample and is in agreement with previous studies. At low temperatures a paramagnetic to antiferromagnetic transition is observed at $T_N = 30.0$ K. Our analysis shows that at $T = 4$ K the two inequivalent Fe sites have antiparallel magnetic moments that are aligned along the a -axis. The average magnetic moment, $gS = 5.0 \mu_B$ indicates homogeneous Fe^{3+} ($S = \frac{5}{2}$). © 2001 Elsevier Science B.V. All rights reserved.

Keywords: Lithium–iron–phosphate; Neutron-diffraction; Antiferromagnet; Phase-transition; Crystal-structure

1. Introduction

$\text{Li}_3\text{Fe}_2(\text{PO}_4)_3$ belongs to a diverse family of ionic conductors of the type $\text{Li}_3\text{M}_2(\text{PO}_4)_3$, where $M = \text{Fe}, \text{Ni}, \text{Cr}, \text{Sc}$, which can be potentially useful for rechargeable batteries [1–4]. The three dimensional (3D) network, in which Li atoms intercalate, consists of $\text{M}_2\text{T}_3\text{O}_{12}$ ($M = \text{Fe}, \text{Cr}, \text{Sc}; T = \text{P}, \text{S}, \text{Si}, \text{Mo}, \text{Ge}$) interconnected polyhedra. In the 3D $\text{M}_2\text{T}_3\text{O}_{12}$ framework, each M atom is at the center of an octahedra surrounded by six oxygen atoms that are situated at the vertices of six TO_4

tetrahedra (at room temperature these polyhedra are slightly distorted) [5]. Such corner sharing octahedra–tetrahedra do not have simple M–O–M or T–O–T bonds, but rather couple transition metal ions through a more complicated M–O–T–O–M path. At room temperature $\text{Li}_3\text{Fe}_2(\text{PO}_4)_3$ can be stabilized in one of the two distinct crystallographic structures [5–7], monoclinic ($\text{P}2_1/n$) or rhombohedral ($\text{R}\bar{3}$) symmetry depending on the method of preparation. If synthesized by the ceramic method, $\text{Li}_3\text{Fe}_2(\text{PO}_4)_3$ assumes a monoclinic phase [5]. The rhombohedral symmetry can be obtained by ion exchange of $\text{Na}_3\text{Fe}_2(\text{PO}_4)_3$ in LiNO_3 aqueous solution [7]. This phase is metastable and by heating the compound to above 570°C it transforms into the monoclinic phase. In

*Corresponding author. Tel.: +1-515-294-6023; fax: +1-515-294-0689.

E-mail address: vaknin@ameslab.gov (D. Vaknin).

the rhombohedral phase, $\text{Li}_3\text{Fe}_2(\text{PO}_4)_3$ has good ionic conductivity, a relatively low transition temperature to the superionic conduction state, and is a potential insertion-electrode in lithium-polymer batteries [2–4,7]. The monoclinic phase ($\text{P}2_1/\text{n}$) is also a common impurity phase in the synthesis of $\text{Li}_{1-3x}\text{Fe}_x\text{NiPO}_4$, the subject of the previous study [8].

X-ray diffraction studies of ceramic $\text{Li}_3\text{Fe}_2(\text{PO}_4)_3$ at room temperature by Bykov et al. [5] showed that the space group symmetry is $\text{P}2_1/\text{n}$ ($\text{P}112_1/\text{n}$) with cell parameters of; $a = 8.562(2)$, $b = 12.005(3)$, $c = 8.612(2)$ Å, $\gamma = 90.51(2)^\circ$ (α - $\text{Li}_3\text{Fe}_2(\text{PO}_4)_3$ phase). At temperatures above $T = 573$ K the system transforms to an orthorhombic γ -phase, and in between these two temperatures the same monoclinic phase with slight modification of Li positions was also observed (β -phase). Recent magnetic susceptibility and the Mössbauer effect studies of α - $\text{Li}_3\text{Fe}_2(\text{PO}_4)_3$ by Goñi et al. [9] showed that the magnetic Fe(III) system undergoes an antiferromagnetic phase transition below $T_N = 29$ K. In addition, it was suggested that the two independent Fe crystallographic sites interact antiferromagnetically, whereas the coupling between Fe moments in the same site is ferromagnetic. We have undertaken the following neutron diffraction studies to determine the magnetic structure of α - $\text{Li}_3\text{Fe}_2(\text{PO}_4)_3$ and also to compare structural parameters with those obtained from X-ray diffraction methods.

2. Experimental details

$\text{Li}_3\text{Fe}_2(\text{PO}_4)_3$ was prepared by the ceramic method. Stoichiometric amounts of $\text{Fe}(\text{NO}_3)_3 \cdot 9\text{H}_2\text{O}$, $\text{H}_2\text{NH}_4\text{PO}_4$ and $\text{LiOH} \cdot \text{H}_2\text{O}$ reagents were homogenized in an agate mortar. The resulting mixture was submitted to three consecutive thermal treatments at 573, 773 and 1073 K, with the corresponding homogenization of the sample following each treatment. The metal ions and phosphorous contents were confirmed by inductively coupled plasma atomic emission spectroscopy (ICP-AES) analysis. The analysis yielded the following weight fractions: Li, 5.0(1); Fe, 27.0(1);

P, 21.8(3) wt%. $\text{Li}_3\text{Fe}_2(\text{PO}_4)_3$ requires: Li, 4.99; Fe, 26.76; P, 22.26 wt%.

The powder sample (~ 4 cm³) was contained in a thin walled vanadium sample-can under an atmosphere of helium and mounted on the cold tip of a two stage closed-cycle helium refrigerator. Temperature measurement and control system were achieved by Lakeshore Si diode sensors connected to a three-term controller and was typically better than ± 0.1 K. Two temperature sensors were used; one mounted on the cold tip and the other on the flange of the vanadium sample can, the latter was used for the sample temperature.

The HBLA spectrometer (Ames Laboratory PRT) at the High Flux Isotope Reactor (HFIR) of the Oak Ridge National Laboratory (ORNL) was used for the diffraction measurements. This is a fixed-initial-energy triple-axis spectrometer operating with wavelength $\lambda = 2.356$ Å, ($E_i = 14.7$ meV). Pyrolytic graphite crystals were used for the double bounce configuration monochromator, for the analyzer and for the $\lambda/2$ filters. Graphite filters were placed between the two monochromator crystals and another set after the second monochromator. This configuration yielded a beam that was practically free of $\lambda/2$ contamination, eliminating the $\lambda/2$ component in the beam to better than one part per 10^6 , as measured on both a Bragg reflection and its zero-structure factor lower order reflection. Throughout the measurements the collimation was kept at $58' - 48' - 40' - \text{sample} - 40' - 68'$. The instrument was operated in the elastic configuration using the graphite analyzer. Data were collected by counting against a neutron monitor detector to correct for variations in reactor flux.

3. Results and discussion

3.1. Crystal structure of $\text{Li}_3\text{Fe}_2(\text{PO}_4)_3$

Fig. 1 shows the diffraction pattern of polycrystalline $\text{Li}_3\text{Fe}_2(\text{PO}_4)_3$ at $T = 300$ and 4 K. The diffraction pattern at low temperatures includes some extra reflections that are characteristic of a superimposed magnetic structure, which disappear above 30 K. It is therefore safe to assume that the

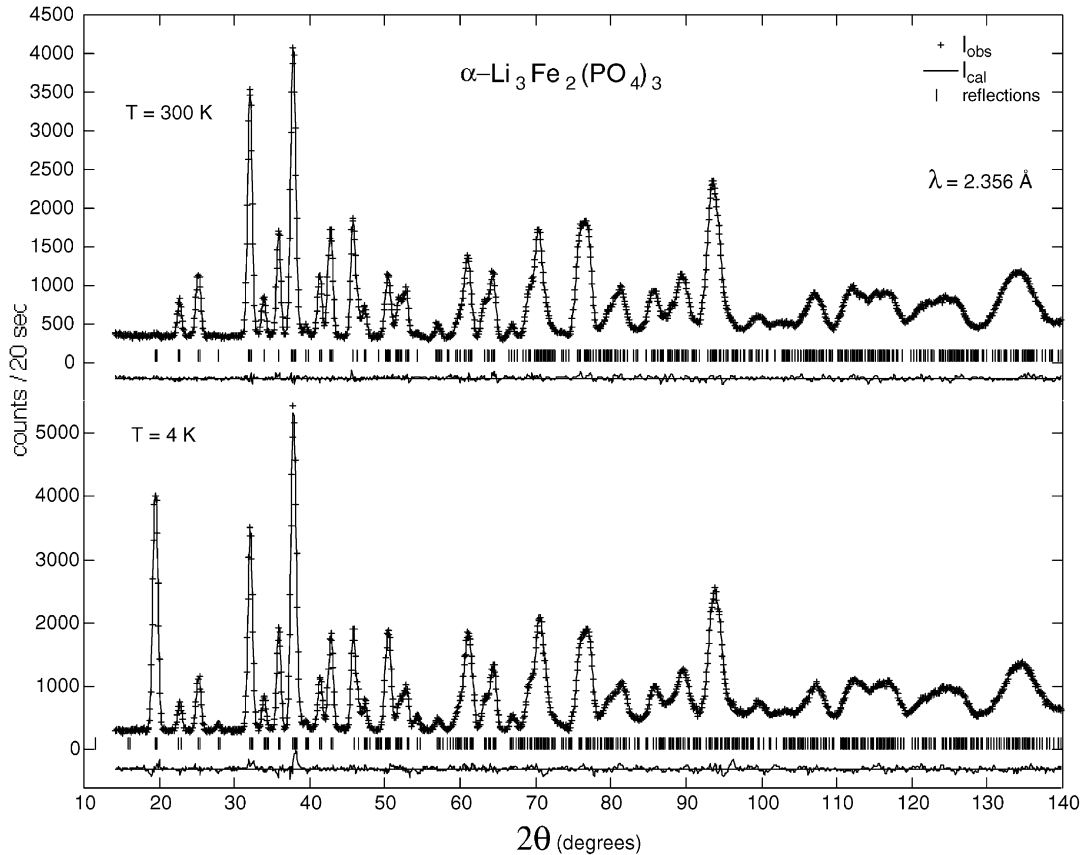


Fig. 1. Neutron powder diffraction patterns of $\text{Li}_3\text{Fe}_2(\text{PO}_4)_3$ at 300 and 4 K. The solid lines through the data are the results of the GSAS Rietveld refinement. Also shown are the locations of the reflections (vertical bars) and the residuals. The data at $T = 4$ K were fitted to a combined structural magnetic model with AF iron moments as discussed in the text.

$T = 300$ K diffraction pattern is dominated by nuclear scattering from chemical structure of $\text{Li}_3\text{Fe}_2(\text{PO}_4)_3$ with no coherent magnetic scattering contribution. GSAS Rietveld refinement routines were used to analyze the data in this experiment [10]. To confirm the phase of the system at 300 K a refinement was attempted using the rhombohedral space group $R\bar{3}$ (the phase of rhombohedral $\text{Li}_3\text{Fe}_2(\text{PO}_4)_3$). The analysis clearly showed that this symmetry was incorrect for the sample studied. The parameters from the Bykov et al. [5] study were used as starting values for the refinement in the present study, using the space group symmetry $P2_1/n$ (specifically $P112_1/n$). This set of parameters consisted of the lattice para-

meters, atomic coordinates and isotropic displacement parameters. Any parameters that could be obtained by direct calculation were fixed, for example; the absorption [13] and peak shape [14] parameters were calculated from a standard sample and the instrument configuration. In addition, some soft “restraints” were imposed on bond lengths [11].

The pseudo-Voigt function for peak profiles was used with coefficients as parameterized by Thompson et al. [12] and asymmetry correction of Finger et al. [13]. A linear interpolation background function was used and the absorption for the sample (attenuation factor) was calculated using the cross-sections of Sears [14].

The following scheme was followed in refining the 300 K data:

1. Soft restraints were imposed on the phosphorus–oxygen bond lengths; $1.540 \pm 0.080 \text{ \AA}$ [11].
2. Lattice parameters, scale factor, background and profile parameters were refined while holding all atomic positions and thermal parameters at the Bykov values.
3. When these parameters were satisfactorily refined, the profile and background parameters were fixed and the atomic positions were varied.
4. After refining the atomic positions, they were fixed and sets of isotropic displacement parameters were allowed to vary; first the oxygens with others fixed, then the iron and phosphorus isotropic displacement parameters were allowed to vary and finally the lithium parameters. Allowing all isotropic displacement parameters to vary simultaneously produced nonphysical values (<0) for several atoms.
5. A final refinement of all atom positions was performed with the isotropic displacement fixed at the values found in Ref. [4].

The scale factor and lattice parameters were allowed to vary in all refinement runs. The resulting fit shown in Fig. 1 appears to be quite good. A caution must be made on assigning too much of physical significance to some of the parameters, especially, the isotropic displacement parameters, and only general trends should be considered.¹

The parameters obtained in this study and those of Bykov et al. are listed in Table 1. The agreement between the neutron diffraction and the X-ray results is remarkable, where differences in parameters can arise from slight differences in sample

Table 1

Structural parameters for monoclinic (space group $P2_1/n$ [$P112_1/n$]) α - $\text{Li}_3\text{Fe}_2(\text{PO}_4)_3$ at $T = 300 \text{ K}$ from Bykov et al. and in italics are from this work

Temperature	300 K Bykov	300 K	4 K	
a (Å)	8.562(2)	<i>8.581(1)</i>	<i>8.571(1)</i>	
b (Å)	12.005(3)	<i>12.033(1)</i>	<i>12.005(1)</i>	
c (Å)	8.612(2)	<i>8.625(1)</i>	<i>8.612(1)</i>	
γ	90.51(2)°	<i>90.41(1)°</i>	<i>90.50(1)°</i>	
ρ calc. (g/cm ³)		<i>3.114</i>	<i>3.129</i>	
R_p		<i>0.0246</i>	<i>0.0338</i>	
R_B (or R_F^2)		<i>0.0166</i>	<i>0.0166</i>	
wR_p		<i>0.0320</i>	<i>0.0395</i>	
χ^2		<i>0.7872</i>	<i>1.664</i>	
Atom	x	y	z	$U_{\text{ISO}} \times 100$ (Å) [2]
Li(1)	0.295(2) <i>0.310(3)</i>	0.322(1) <i>0.327(3)</i>	0.276(2) <i>0.259(4)</i>	1.5(2) 2.491
Li(2)	0.577(2) <i>0.580(4)</i>	0.193(1) <i>0.211(3)</i>	0.421(2) <i>0.404(4)</i>	2.4(3) 3.184
Li(3)	0.912(2) <i>0.891(5)</i>	0.241(2) <i>0.246(4)</i>	0.297(2) <i>0.287(4)</i>	4.1(4) 4.562
Fe(1)	0.2461(1) <i>0.245(1)</i>	0.1072(1) <i>0.1020(5)</i>	0.4606(1) <i>0.4599(7)</i>	0.61 0.583
Fe(2)	0.7534(1) <i>0.759(1)</i>	0.3943(1) <i>0.3893(6)</i>	0.4703(1) <i>0.4692(8)</i>	0.59 0.832
P(1)	0.1040(2) <i>0.101(1)</i>	0.1490(2) <i>0.148(1)</i>	0.1044(2) <i>0.109(1)</i>	0.58 1.354
P(2)	0.6029(2) <i>0.606(1)</i>	0.3509(1) <i>0.348(1)</i>	0.1150(2) <i>0.120(1)</i>	0.55 0.253
P(3)	0.0350(2) <i>0.0318(9)</i>	0.4937(2) <i>0.488(1)</i>	0.2478(2) <i>0.253(1)</i>	0.62 0.700
O(1)	0.4278(6) <i>0.427(1)</i>	0.3319(4) <i>0.3307(8)</i>	0.0915(6) <i>0.099(1)</i>	1.10 1.618
O(2)	0.9251(6) <i>0.920(1)</i>	0.1497(4) <i>0.147(1)</i>	0.1119(9) <i>0.110(2)</i>	1.15 0.620
O(3)	0.3502(6) <i>0.364(2)</i>	0.2636(5) <i>0.260(1)</i>	0.4811(7) <i>0.491(2)</i>	1.29 1.330
O(4)	0.8062(6) <i>0.795(1)</i>	0.2205(4) <i>0.218(1)</i>	0.4971(6) <i>0.499(1)</i>	1.05 1.454
O(5)	0.1693(7) <i>0.159(2)</i>	0.0379(5) <i>0.037(1)</i>	0.0574(8) <i>0.050(2)</i>	1.53 1.761
O(6)	0.6465(6) <i>0.641(2)</i>	0.4721(4) <i>0.470(1)</i>	0.0907(6) <i>0.082(1)</i>	1.09 1.007
O(7)	0.4500(6) <i>0.445(2)</i>	0.0683(4) <i>0.064(1)</i>	0.3676(6) <i>0.362(2)</i>	1.17 1.213
O(8)	0.9263(5) <i>0.917(2)</i>	0.4028(4) <i>0.401(1)</i>	0.3142(6) <i>0.316(1)</i>	1.34 1.944
O(9)	0.1715(6) <i>0.166(1)</i>	0.4325(5) <i>0.427(1)</i>	0.1684(7) <i>0.176(1)</i>	1.32 1.169
O(10)	0.6017(7) <i>0.601(1)</i>	0.0704(5) <i>0.0656(9)</i>	0.1304(8) <i>0.123(2)</i>	1.38 1.099
O(11)	0.1613(6) <i>0.165(1)</i>	0.1864(4) <i>0.185(1)</i>	0.2654(6) <i>0.266(1)</i>	1.03 0.964
O(12)	0.6400(6) <i>0.628(1)</i>	0.3162(4) <i>0.3112(9)</i>	0.2824(6) <i>0.290(2)</i>	1.02 2.026

¹ Technical notes for the Rietveld refinement

Linear attenuation factor = 0.776 cm^{-1}

Linear interpolation function (#7) in GSAS (Ref. [10]).

Lorentzian parameters

$S/L = 0.03236$ (sample height/ S - D distance)

$H/L = 0.06165$ (detector height/ S - D distance)

Peak profile type no. 3 Number of coefficients: 8

Pseudovoigt profile coefficients as parameterized in

Ref. [15]. Asymmetry correction of Finger et al. Ref. [16].

Cut-off for peaks is 0.30 percent of the maximum [17].

preparations. In agreement with the observation by Bykov et al., Li(3) has probably the highest mobility, as indicated by its large displacement factor ($U = 0.046 \text{ \AA}^2$ [2]). However, the neutron diffraction results indicate that the displacement factors of the light atoms (Li and O) are systematically higher than those obtained in the X-ray studies.

3.2. Magnetic structure

Fig. 2 shows the difference between the diffraction pattern at $T = 40$ and 4 K , where a new set of reflections can be indexed using the chemical unit cell. The lowest order reflection at $2\theta = 19.5^\circ$ can be indexed as a superposition of the (110) and (011) Bragg reflections, which for the chemical structure both have negligibly small structure

factors. Due to the closeness of the a and c lattice parameters, these two peaks could not be resolved with the setup of our spectrometer. Other peaks shown in Fig. 2, such as the one at $2\theta = 37.9^\circ$ can be indexed as $(\bar{1}12)$, $(\bar{2}11)$, (112) , (211) , $(\bar{1}30)$, (130) and (031) reflections and are superimposed on the same reflections from the chemical unit cell. To account for the new reflections observed at low temperature we follow the suggestion by Goñi et al. [9] that the iron system undergoes an antiferromagnetic ordering.

The GSAS Rietveld analysis of the 4 K data proceeded in a similar fashion to that of the 300 K data with two exceptions. First, magnetic moments were included on the Fe sites. Second, the isotropic displacement parameters from the 300 K Rietveld analysis were used to calculate the vibrational frequencies (ν) for the atomic species

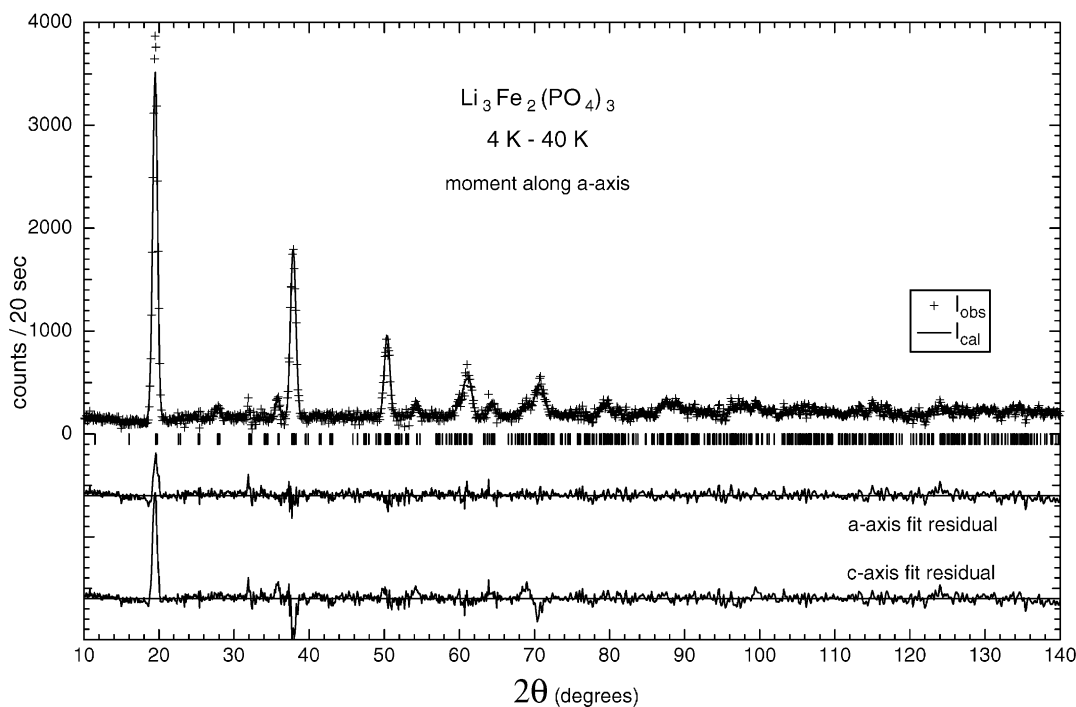


Fig. 2. Difference plot of diffraction patterns of $\text{Li}_3\text{Fe}_2(\text{PO}_4)_3$ at 4 and 40 K, showing the magnetic contribution to scattered intensity, (200 counts have been added to bring all counts > 0). Thermal factors of the Bragg reflections and crystallographic changes (for instance, lattice parameters) are very minute between the two temperatures as evidenced by the symmetric magnetic Bragg reflections. Therefore, this difference is a valid representation of magnetic diffraction alone. The solid line is a fit to the AF model shown in Fig. 3b. The residuals of the fits with moments along the a -axis (Fig. 3b) and along the c -axis (Fig. 3a) are shown for comparison.

using the expression [18,19]

$$U_{\text{iso}} = \langle u^2 \rangle = h / (8\pi^2 m v) \coth(hv / 2k_B T). \quad (1)$$

These frequencies were then used in Eq. (1) to calculate U_{iso} at 4 K. For the 4 K Rietveld refinement the isotropic displacements were held fixed at these values.

The unit cell of $\text{Li}_3\text{Fe}_2(\text{PO}_4)_3$ has four atoms at each of two Fe sites. Reasonable fits to the data were achieved with models in which the four Fe atoms of one type have moments parallel to either the c -axis or a -axis and the four moments on the other Fe site antiparallel to the former (shown in Fig. 3). The propagation vector can be along the (010) direction, but no peak is observed at this Bragg point due to the small structure factor. Despite its complicated structure $\text{Li}_3\text{Fe}_2(\text{PO}_4)_3$ is nearly tetragonal so that the two models (moments along the a -axis and c -axis) predict peaks in the same unresolved-regions in the powder pattern, but with different structure factors. The quality of the fit using the moments parallel and antiparallel to the a -axis was noticeably better, however. The least squares refinement using the GSAS routines, with moments either along the a - or c -axis, yielded an average magnetic moment per iron site $gS = 5.0 \pm 0.2 \mu_B$. Assuming a $g = 2.0$, this is in good agreement with the expected electronic configuration of iron in $\text{Li}_3\text{Fe}_2(\text{PO}_4)_3$ as Fe^{3+} and $S = 5/2$.

As an additional check of the magnetic model, we refined the magnetic structure using the difference data shown in Fig. 2. We found that thermal factors of Bragg reflections and crystallographic changes (for instance, lattice parameters) are very minute between the $T = 4$ and 40 K, as also evidenced by the symmetric magnetic Bragg reflections (Fig. 2). Therefore, this difference is a valid representation of magnetic diffraction only, and justifies the refinement of the magnetic model only, eliminating the nuclear contribution from the diffraction pattern. The solid line in Fig. 2, is the GSAS refinement using the AF model shown in Fig 3b with the moments along the a -axis. The residuals from fits to the AF model with moments along the a -axis and along the c -axis are also shown in Fig. 2. It is clear that the fit with the

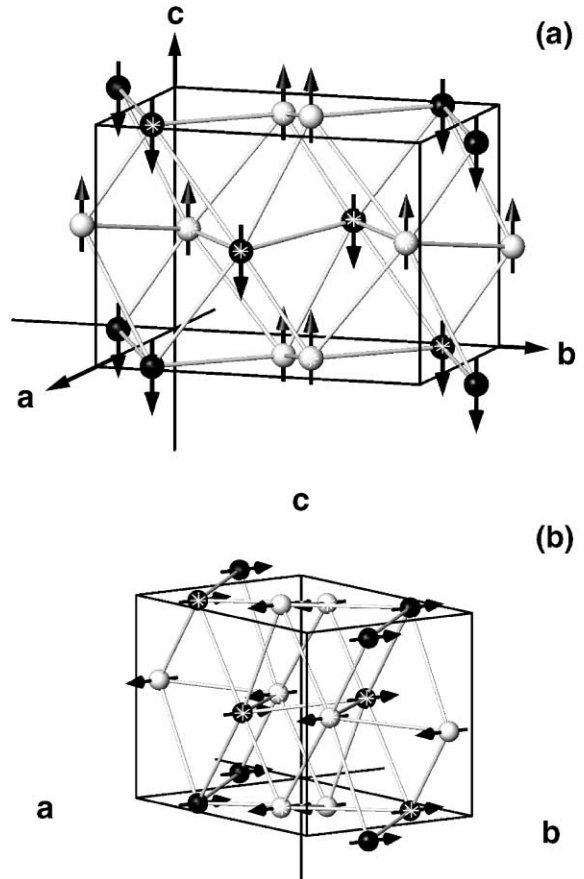


Fig. 3. Magnetic model of $\alpha\text{-Li}_3\text{Fe}_2(\text{PO}_4)_3$ with two types of Fe atoms and their respective moments (a, along the c -axis and b, along the a -axis). Atoms marked with an asterisk are inside the indicated unit cell. Although both models predict similar pattern within the resolution of the spectrometer, the more plausible model according to our analysis is the one with the magnetic moments aligned along the a -axis, which yields a better fit to the data.

moments along the a -axis is of better quality than the one with the moments along the c -axis.

The square root of the normalized intensity of the magnetic peak at $2\theta = 19.5^\circ$ is proportional to the order parameter, in this case the sublattice magnetization $M(T)$. Fig. 4 shows the temperature dependence of the order normalized intensity together with a fit to the data using the power law

$$M(T)/M(0) = A(1 - T/T_N)^{2\beta}. \quad (2)$$

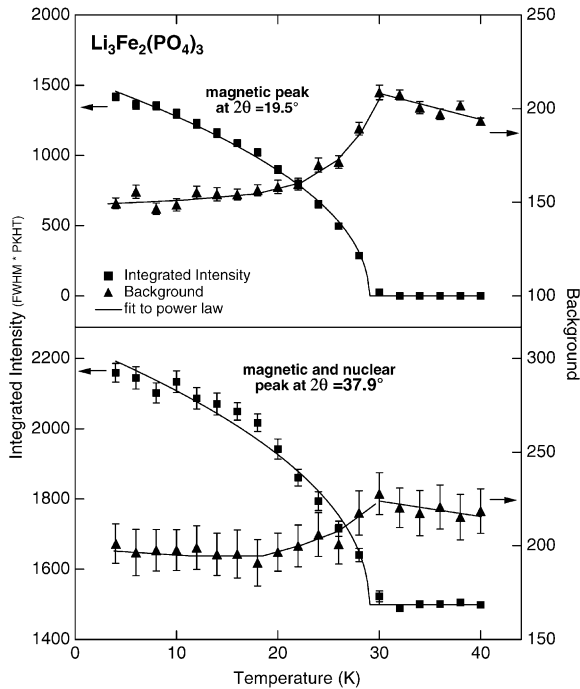


Fig. 4. Integrated intensity (squares) and background as a function of temperature for the first magnetic peak (upper plot) and the first nuclear peak with significant intensity increase (lower plot) (FWHM is the full width at half maximum and PKHT is the peak height). Shown as a solid line, is a fit of the magnetic peak intensity to a power law expression. Contributing reflections to the magnetic peak are the $(\bar{1}10)$, (011) and (110) reflections and for the mixed peak, the $(\bar{1}12)$, (211) , (112) , (211) , $(\bar{1}30)$, (130) and (031) reflections. Critical scattering (triangles) measured by the background near the magnetic peaks indicating a transition temperature $T_N = 30$ K and critical fluctuations that persist above the transition.

The best-fit parameters yield a critical exponent $\beta = 0.27 \pm 0.02$ and a Néel temperature of $T_N = 30.0 \pm 0.1$ K. The temperature behavior of the peaks at $2\theta = 39.7^\circ$ is practically the same as that of the peak at $2\theta = 19.5^\circ$, as shown in Fig. 4b confirming the common origin of these peaks. The critical exponent β is significantly smaller than that expected for the mean field model ($\beta = 0.5$), the 3D Heisenberg or the Ising model ($\beta \approx 0.33$). This might be due to the distribution in the magnetic coupling among the nearest-neighbor iron moments. The Fe–Fe magnetic coupling is not the common superexchange via oxygen Fe–O–Fe, but a coupling through the more complicated (dis-

torted) octahedra–tetrahedra vertices Fe–O–P–O–Fe, with a distribution of bond lengths that vary from one site to another. The first shell of eight iron neighbors coupled to a central Fe through the Fe–O–P–O–Fe are at distances that vary from 4.7 to 5.5 Å. Such a distribution in bond lengths might lead to a distribution in the magnetic coupling between iron moments and consequently lead to a lower exponent β as observed in this study.

The critical fluctuations as measured by the background near the magnetic peaks are shown in Fig. 4 (triangles), with a clear transition at $T = 30$ K. The decay of this scattering above the transition is much more gradual compared to that below the transition, indicating the development of short-range magnetic order at higher temperatures. This can be studied more thoroughly with a single crystal which is not available to us at this time. In preparing Fig. 2 by subtraction of the $T = 4$ K data from the 40 K data, the resulting difference scan had negative background. In general, we found, as also can be seen in Fig. 1, that the overall background level is reduced significantly below the AF transition. This abrupt change observed around the transition suggests that the significant contribution to the RT background is due to the incoherent scattering from the magnetic system in either the paramagnetic disordered state or at the short-range order regime.

4. Conclusions

The present neutron diffraction study confirms the findings of Goñi et al. regarding the antiferromagnetic nature of α - $\text{Li}_3\text{Fe}_2(\text{PO}_4)_3$ (Ref. [4]). The magnetic structure is such that the four Fe atoms of one type have moments parallel to the a -axis and the four moments on the other Fe site antiparallel to the former (Fig. 3b). The Mössbauer spectra as well as the neutron diffraction refined magnetic model indicate that the ground state of this system is AF with one type of moment in both iron sites, Fe^{3+} ($S = 5/2$). The temperature behavior of the order parameter, the Mössbauer spectra and the magnetic susceptibility all indicate some subtleties in the magnetic behavior that are characteristic of a

magnetic system with slight disorder. This behavior can be the result of the complicated exchange coupling due to the nonuniform Fe–O–P–O–Fe bonding between nearest-neighbor (NN) spins, J_{ij} . The exchange in this case is antiferromagnetic in nature but it varies in magnitude from site to site, with a plausible simplified 3D Hamiltonian of the form

$$-\sum J_{ij} S_i \cdot S_j, \quad J_{ij} = -J_0 + \Delta_{ij}, \quad |J_0| \gg |\Delta_{ij}|, \quad (3)$$

where Δ_{ij} varies within the NN sphere.

Acknowledgements

Ames Laboratory is operated for the US Department of Energy by Iowa State University under Contract No. W-7405-Eng-82. The Director for Energy Research, Office of Basic Energy Sciences, supported the work at Ames. ORNL is managed for the US Department of Energy by UT-Battelle, LLC under contract DE-AC05-00OR22725.

References

- [1] T. Kanazawa, *Inorganic Phosphate Materials*, Elsevier, Tokyo, 1993.
- [2] C. Masquelier, A.K. Padhi, K.S. Nanjundaswamy, J.B. Goodenough, *J. Solid State Chem.* 135 (1998) 228.
- [3] A.K. Cheetam, *Science* 264 (1994) 794.
- [4] C. Julien, G.A. Nazri, *Solid State Batteries: Materials Design and Optimization*, Kluwer Academic Publishers, Boston, MA, 1994.
- [5] A.B. Bykov, A.P. Chirkin, L.N. Demyanets, S.N. Doronin, E.A. Genkina, A.K. Ivanov-Shits, I.P. Kondratyuk, B.A. Maksimov, O.K. Mel'nikov, L.N. Muradyan, V.I. Simonov, V.A. Timofeeva, *Solid State Ionics* 38 (1990) 31.
- [6] F. d'Yvoire, M. Pintard-Scrépel, E. Bretey, M. De La Rochère, *Solid State Ionics* 9 & 10 (1983) 851.
- [7] C. Masquelier, C. Wurm, J. Rodríguez-Carvajal, J. Gaubicher, L. Nazar, *Chem. Mater.* 12 (2000) 525.
- [8] D. Vaknin, J.L. Zarestky, J.E. Ostenson, B.C. Chakoumakos, A. Goñi, P.J. Pagliuso, T. Rojo, G.E. Barberis, *Phys. Rev. B* 60 (1999) 1100.
- [9] A. Goñi, L. Lezama, N.O. Moreno, L. Fournés, R. Olazcuaga, G.E. Barberis, T. Rojo, *Chem. Mater.* 12 (2000) 62.
- [10] A.C. Larson, R.B. Von Dreele, M. Lujan Jr., computer code GSAS, Generalized Structure Analysis System, Neutron Scattering Center, Los Alamos National Laboratory, 1990.
- [11] A.J.C. Wilson (Ed.), *International Tables for Crystallography*, Kluwer, Academic Publishers, Dordrecht, 1992.
- [12] P. Thompson, D.E. Cox, J.B. Hastings, *J. Appl. Cryst.* 20 (1987) 79.
- [13] L.W. Finger, D.E. Cox, A.P. Jephcoat, *J. Appl. Cryst.* 27 (1994) 892.
- [14] V.F. Sears, *Neutron News* 3 (3) (1992) 29.
- [15] P. Thompson, D.E. Cox, J.B. Hastings, *J. Appl. Cryst.* 20 (1987) 79–83.
- [16] L.W. Finger, D.E. Cox, A.P. Jephcoat, *J. Appl. Cryst.* 27 (1994) 892–900.
- [17] A.S. Andersson, B. Kalska, P. Jönsson, L. Häggström, P. Nordblad, R. Tellgren, J.O. Thomas, *Chem.* 10 (2000) 2542.
- [18] T.M. Tritt (Ed.), *Recent Trends in Thermoelectric Materials Research II; Semiconductors and Semimetals*, Academic Press, New York, 2001.
- [19] B.T.M. Willis, A.W. Pryor, *Thermal Vibrations in Crystallography*, Cambridge University Press, Cambridge, 1975, p. 280.